

Glass-like Cross-plane Thermal Conductivity of Kagome Metals RbV₃Sb₅ and CsV₃Sb₅

Yu Pang¹, Jinjin Liu^{2,5}, Zeyu Xiang¹, Xuanhui Fan³, Jie Zhu^{3,*}, Zhiwei Wang^{2,5,6,*}, Yugui Yao^{2,5,6}, Xin Qian^{1,*}, Ronggui Yang^{1,4,*}

¹ School of Energy and Power Engineering, Huazhong University of Science and Technology, Wuhan 430074, China

² Centre for Quantum Physics, Key Laboratory of Advanced Optoelectronic Quantum Architecture and Measurement (MOE), School of Physics, Beijing Institute of Technology, Beijing 100081, China

³ School of Energy and Power Engineering, Dalian University of Technology, Dalian 116024, China

⁴ State Key Laboratory of Coal Combustion, Huazhong University of Science and Technology, Wuhan 430074, China

⁵ Beijing Key Lab of Nanophotonics and Ultrafine Optoelectronic Systems, Beijing Institute of Technology, Beijing 100081, China

⁶ Material Science Center, Yangtze Delta Region Academy of Beijing Institute of Technology, Jiaxing 314011, China

*Corresponding emails: zhujie@dlut.edu.cn; zhiweiwang@bit.edu.cn; xinqian21@hust.edu.cn; ronggui@hust.edu.cn

Abstract

This work reports the thermal conductivity of RbV₃Sb₅ and CsV₃Sb₅ with three-dimensional charge density wave phase transitions from 80 K to 400 K measured by pump-probe thermoreflectance techniques. At room temperature, the in-plane (basal plane) thermal conductivities are found moderate, i.e., 12 W m⁻¹ K⁻¹ of RbV₃Sb₅ and 8.8 W m⁻¹ K⁻¹ of CsV₃Sb₅, and ultralow cross-plane (stacking direction) thermal conductivities are observed, with 0.72 W m⁻¹ K⁻¹ of RbV₃Sb₅ and 0.49 W m⁻¹ K⁻¹ of CsV₃Sb₅ at 300 K. A unique glass-like temperature dependence in the cross-plane thermal conductivity is discovered, which decreases monotonically even lower than the Cahill-Pohl limit as the temperature decreases below the phase transition point T_{CDW} . This temperature dependence is found to obey the hopping transport picture. In addition, a peak in cross-plane thermal conductivity is observed at T_{CDW} as a fingerprint of the modulated structural distortion along the stacking direction.

Two-dimensional kagome lattice is a topological system with flat electronic bands, Dirac cones, and Van Hove singularities^{1,2}, which induce many intriguing physical phenomena such as spin liquid states³, bond density wave order⁴, superconductivity⁵ and charge density wave (CDW)⁶. The recently discovered layered kagome metals AV_3Sb_5 ($A = K, Rb, Cs$)⁷ with \mathbb{Z}_2 -type nontrivial band topology^{8,9} provide a unique platform for studying electron correlations, topological effects, and quantum phase transition^{10,11}. Particularly, AV_3Sb_5 exhibits lots of interesting phenomena, such as anomalous Hall effects¹², spontaneous symmetry breaking¹³, competition between CDW with superconductivity¹⁴⁻¹⁶, etc.

The CDW in AV_3Sb_5 is featured by simultaneous lattice distortions both in each basal plane and the modulated stacking of different distortion patterns^{17,18}. Recent measurements on magnetization, heat capacity, and electrical resistivity identify that AV_3Sb_5 undergoes a first-order CDW phase transition at the critical temperatures $T_{CDW} \approx 78-102$ K^{8,9,19}. Above the CDW transition ($T > T_{CDW}$), the crystal structure of AV_3Sb_5 consists of a high-symmetry vanadium-based kagome sublattice, as shown in Fig. 1a-b. However, density functional theory (DFT) study predicts that the high-symmetry structure exhibits phonon instability below T_{CDW} , as softening acoustic phonon modes emerge near M and L points in the Brillouin zone²⁰. The soft phonon modes drive the vanadium atoms in each kagome layer spontaneously shift away from the high-symmetry sites, forming 2×2 superlattices with the star of David (SD) or inverse star of David (ISD) patterns²⁰. More interestingly, DFT study further predicts that lattice distortion happens not only inside the basal planes but such distortion is modulated with a stacking period of 2 or 4 layers^{18,20}. The 2×2 in-plane superlattice is observed earlier using both XRD⁸ and scanning tunneling microscopy (STM)²¹⁻²³. Recently, a variety of experimental measurements further confirm multiple superstructures of 3D CDW ordering, such as $2 \times 2 \times 2$ ¹⁷, $2 \times 2 \times 4$ ¹⁸, or even both²⁴, etc. Despite these discoveries, origin of the 3D CDW in AV_3Sb_5 remains elusive. A dilemma is that inelastic X-ray scattering shows the absence of clear phonon softening or Kohn anomaly²⁵, which is contradictory to DFT predictions²⁰. In addition, Subires *et al.* recently proposed that CDW phase change in AV_3Sb_5 is of order-disorder type which goes beyond the conventional weak-coupling regime of Peierls transitions²⁶.

Characterizing thermal properties could provide a unique angle to study the mechanisms of CDW phase transition. For example, thermal conductivity shows a peak or a sudden drop

near T_{CDW} . In CDW materials with one-dimensional (1D) lattice distortions such as $\text{K}_{0.3}\text{MoO}_3$ and $(\text{TaSe}_4)_2\text{I}^{27}$, a peak in temperature-dependent thermal conductivity is usually observed near the phase transition point T_{CDW} , due to the excess heat carried by phasons or amplitudons as quantized modes of CDW²⁸. In layered materials such as 1T-TaS₂, and 2H-TaSe₂^{29,30} with two-dimensional (2D) lattice distortions, strong electron-phonon interactions driving the phase transition are also manifested in a sudden drop in thermal conductivity near T_{CDW} due to the additional scattering of heat-carrying phonons. Till now, 3D CDW has only been identified in a few systems such as $\text{YBa}_2\text{Cu}_3\text{O}_{6.67}$ ³¹ and 1T-VSe₂³² other than AV_3Sb_5 , while how 3D lattice distortions affect thermal transport remains largely unexplored. Recently, Yang *et al.* reported a glass-like in-plane thermal conductivity in AV_3Sb_5 due to charge fluctuations above T_{CDW} ³³, but measurements of cross-plane thermal conductivity near the CDW transition are still in urgent need for a complete understanding of thermal transport in layered AV_3Sb_5 with 3D CDW.

In this work, temperature-dependent thermal conductivity along the cross-plane direction of kagome metals (RbV_3Sb_5 and CsV_3Sb_5) are measured using the pump-probe thermoreflectance technique³⁴. This work observes that AV_3Sb_5 exhibits a unique glass-like temperature dependence in the cross-plane thermal conductivity, where the thermal conductivity drops rapidly with decreasing temperatures lower than the Cahill-Pohl limit³⁵ at temperatures below T_{CDW} . A hopping model is proposed to explain this trend. In addition, a peak at the T_{CDW} is observed in the temperature-dependent cross-plane thermal conductivity. Our observation of the glass-like cross-plane thermal conductivity aligns with the recent discovery that the CDW transition in AV_3Sb_5 is three-dimensional and is of order-disorder type beyond the conventional weak-coupling regime^{17,26}.

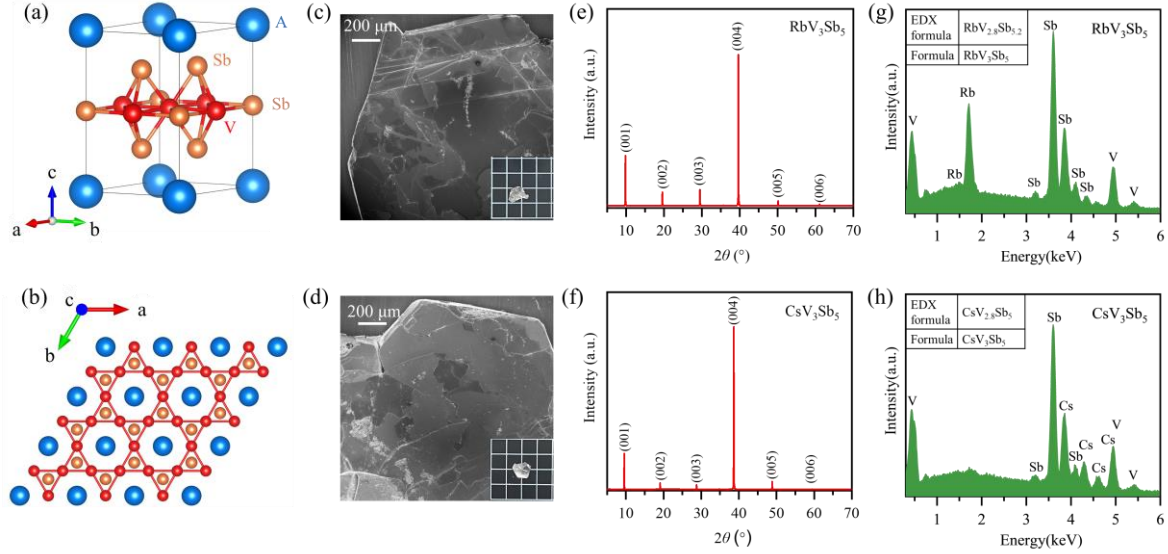


Fig. 1. (a) Unit cell of AV₃Sb₅, (A = K, Rb, Cs) (b) atomic structure of AV₃Sb₅ projected to the (001) plane. A, V, and Sb atoms are presented as blue, red, and orange balls, respectively. SEM and optical (inset) images of (c) RbV₃Sb₅ and (d) CsV₃Sb₅. Insets show the optical image of the corresponding materials, and each grid in the optical image is 3 mm by 3 mm. XRD and EDX characterization of (e-g) RbV₃Sb₅ and (f-h) CsV₃Sb₅.

Single crystals of RbV₃Sb₅ and CsV₃Sb₅ are prepared with binary Rb-Sb and Cs-Sb fluxes using the self-flux method³⁶. Alkali metals (Rb and Cs, Alfa Aesar, 99.8%), vanadium pieces (Aladdin, 99.97%), and Sb (Alfa Aesar, 99.9999%) with a molar ratio of 9: 3: 17 are loaded into an alumina crucible and sealed in an evacuated quartz tube. These raw materials are heated at 5 K/min and kept at 1273 K for 24 h. After that, the ampoules are cooled down to 473 K at 3 K/h. The residual flux is removed using deionized water. The morphology of the synthesized samples is characterized by scanning electron microscope (SEM), as shown in Fig. 1c-d. XRD characterizations are shown in Fig. 1e-f. The full width at half maxima (FWHM) of the diffraction peaks on the (00*l*) crystal plane of the two samples are both nearly 0.07°, indicating good crystallinity of the synthesized samples. Energy dispersive X-ray spectroscopy (EDX) results suggest that the samples crystallize in RbV_{2.8}Sb_{5.2} (Fig. 1g) and CsV_{2.8}Sb₅ (Fig. 1h), respectively, which agree well with nominal compositions (inset, Figs. 1g and 1h).

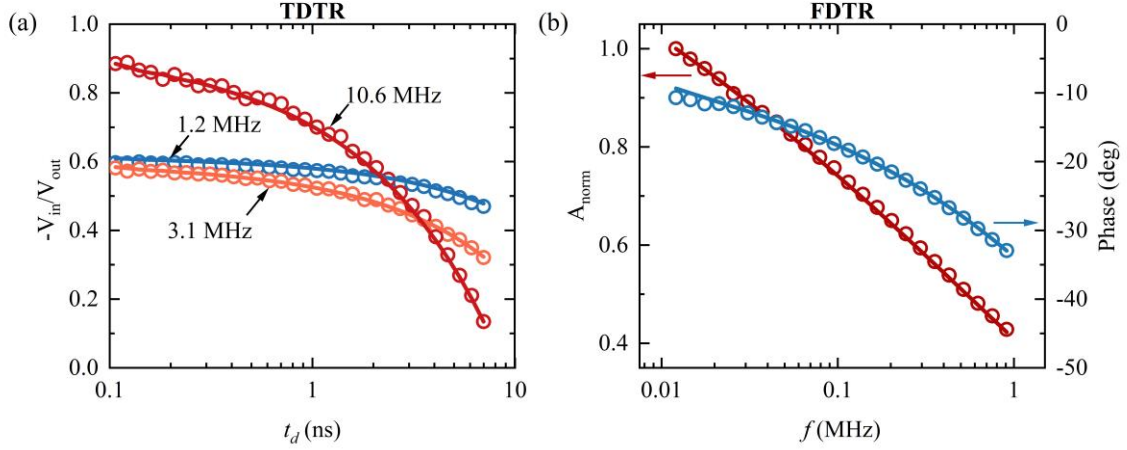


Fig. 2. (a) TDTR and (b) FDTR experimental signals (open symbols) at room temperature along with the fitting curves calculated based on the heat transfer model. The TDTR signals $-V_{in}/V_{out}$ are acquired using an identical large beam size ($w = 20 \mu\text{m}$) and different modulation frequencies $f = 1.2, 3.1,$ and 10.6 MHz . The FDTR data were taken from low modulation frequency range $f = 0.1\text{-}1 \text{ MHz}$, with the A_{norm} and phase signals being both well-fitted.

Time-domain thermoreflectance (TDTR)³⁷ and frequency-domain thermoreflectance (FDTR) techniques³⁸ are used to measure the room-temperature cross-plane and in-plane thermal conductivity (κ_z and κ_r) of AV_3Sb_5 , respectively. Fig. 2a shows typical TDTR signals of the CsV_3Sb_5 sample using a root-mean-square spot radius of $20 \mu\text{m}$ and multiple modulation frequencies of 1.2 to 10.6 MHz. In this case, the heat transfer is quasi-one-dimensional in the cross-plane direction, and the TDTR signal is only sensitive to κ_z . The cross-plane thermal conductivity κ_z and the interface conductance G are the fitting parameters in data reduction. We found that a single set of κ_z and G can achieve nice fitting of signals at different frequencies, suggesting no modulation frequency dependence originated from non-Fourier phonon transport or local nonequilibrium effects³⁹. The κ_z is determined as $0.49 \pm 0.07 \text{ W m}^{-1} \text{ K}^{-1}$ at room temperature using TDTR with large spot radius ($\sim 20 \mu\text{m}$). After κ_z is determined, in-plane thermal conductivity κ_r is measured as $8.8 \pm 1.5 \text{ W m}^{-1} \text{ K}^{-1}$ using FDTR technique. A tightly focused spot radius of $3 \mu\text{m}$ and low modulation frequency range $f = 0.01\text{-}1 \text{ MHz}$ is used when performing FDTR measurements to ensure high sensitivity to κ_r , as shown in Fig. 2b. Similarly, κ_z and κ_r of RbV_3Sb_5 at room temperature are also measured as $0.72 \pm 0.10 \text{ W m}^{-1} \text{ K}^{-1}$ and $12 \pm 2 \text{ W m}^{-1} \text{ K}^{-1}$, respectively. Our measurement of κ_r is consistent with the recently report value^{12,33}. More details about pump-probe measurement,

sensitivity analysis, and uncertainty analysis are listed in Supplemental Materials S1-3.

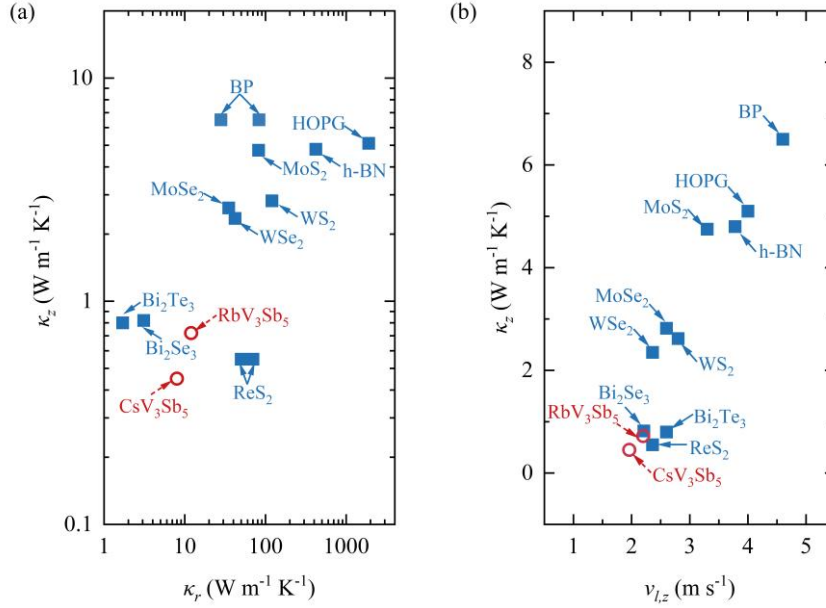


Fig. 3. (a) Summary of experimentally measured cross-plane thermal conductivity κ_z and in-plane thermal conductivity κ_r of layered crystalline materials at room temperature. (b) Collected cross-plane thermal conductivity κ_z of layered crystalline materials versus longitudinal sound velocity $v_{l,z}$. The cross-plane thermal conductivities come from BP⁴⁰, HOPG⁴¹, h-BN⁴², transition metal dichalcogenides (MoS₂, WS₂, MoSe₂, WSe₂)³⁹, ReS₂⁴³, and bismuth dichalcogenides (Bi₂Te₃, Bi₂Se₃)^{44,45}, as well as kagome metals AV₃Sb₅ (A = Rb, Cs) measured in this work. The longitudinal sound velocity $v_{l,z}$ is obtained through phonon dispersion or experimentally determined data. The data of longitudinal sound velocities are taken from BP⁴⁰, HOPG⁴⁶, h-BN⁴², transition metal dichalcogenides (MoS₂, WS₂, MoSe₂, WSe₂)⁴⁷, ReS₂⁴⁸, bismuth dichalcogenides (Bi₂Te₃, Bi₂Se₃)^{49,50}, and kagome metals AV₃Sb₅ (A = Rb, Cs)²⁰.

We compare room-temperature κ_z and κ_r of AV₃Sb₅ in Fig. 3a, as well as other typical van der Waals materials. Among the materials gathered, AV₃Sb₅ exhibits the lowest κ_r other than bismuth dichalcogenides (Bi₂Te₃, Bi₂Se₃), while CsV₃Sb₅ even displays the lowest κ_z . Fig. 3b summarizes the longitudinal sound velocity in the cross-plane and measured κ_z of collected materials. The $v_{l,z}$ of AV₃Sb₅, which are 1960 m s^{-1} and 2200 m s^{-1} for CsV₃Sb₅ and RbV₃Sb₅, respectively, are also relatively low against other layered materials (e.g., $v_{l,z} = 2360 \text{ m s}^{-1}$ for ReS₂⁴³ and $v_{l,z} = 2210 \text{ m s}^{-1}$ for Bi₂Se₃⁴⁹). The low $v_{l,z}$ indicates that the low κ_z of AV₃Sb₅ at room temperature is mainly caused by the weak interlayer bonding strength.

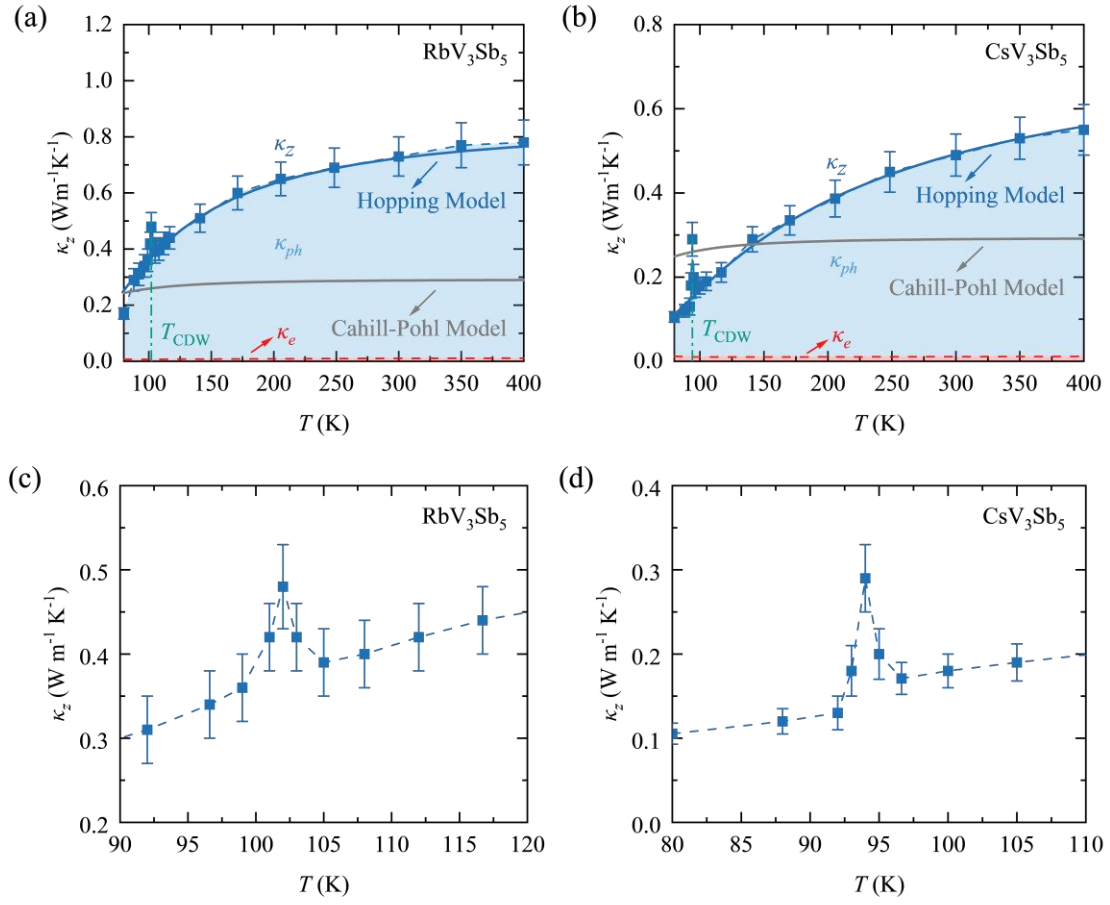


Fig. 4. Measured cross-plane thermal conductivity (a) κ_z of RbV_3Sb_5 and (b) κ_z of CsV_3Sb_5 , over the temperature range of 80-400 K, as well as electron/phonon-contributed terms. Thermal conductivity due to electrons κ_e is obtained using the Wiedemann-Franz law, with phonon thermal conductivity κ_{ph} acquired through subtracting κ_e from the measured thermal conductivity κ . Discrete points, red dotted lines, and middle coloring sections represent the κ , κ_e , and κ_{ph} , respectively, together with cyan dot-dash line lines used for highlighting the T_{CDW} . The blue solid lines are estimated phonon thermal conductivity along cross-plane direction based on the hopping model. The gray solid lines are lower limit to thermal conductivity estimated by the Cahill-Pohl model. (c-d) Details for the peak in κ_z around T_{CDW} for (c) RbV_3Sb_5 and (d) CsV_3Sb_5 .

Figure 4a-b show the temperature-dependent κ_z (80-400 K) of RbV_3Sb_5 and CsV_3Sb_5 , as well as the electron and phonon contributions estimated using the Wiedemann-Franz law (see Supplementary Materials S4). Our measurement shows that electron contribution is negligible in the cross-plane direction, which is typical for layered materials due to the weak interlayer coupling and low charge mobilities in the cross-plane direction⁵¹. Interestingly, the cross-plane

thermal conductivity κ_z shows a glass-like temperature dependence with thermal conductivity increasing monotonically with the temperature. The thermal conductivity even drops below the Cahill-Pohl limit below T_{CDW}^{35} . Our observation is aligned with the observation that localized phonon modes drive structural fluctuations near T_{CDW}^{26} . Considering these localized modes could be well-described by Einstein oscillators, we proposed a hopping model to describe the cross-plane thermal transport. In general, the lattice thermal conductivity of crystalline solids can be expressed as a frequency-dependent integral over the phonon spectrum:

$$\kappa_{ph}(T) = \int C(\omega)D(\omega)d\omega \quad (1)$$

where $C(\omega) = \hbar\omega g(\omega) \frac{\partial f}{\partial T}$ is the spectral volumetric specific heat, with f the Bose-Einstein distribution and $g(\omega)$ the density of states, and $D(\omega)$ is spectral diffusivity for each vibration. In this work, the dispersion of propagating low-frequency phonons is described by the Callaway model⁵², while localized high-frequency modes are treated as Einstein oscillators. The $D(\omega)$ of propagating modes is described as $v(\omega)^2\tau(\omega)/3$ using the phonon-gas model, where v is group velocity and τ is relaxation time. For the localized modes, the transport process is described by a hopping model, with hopping length α , hopping rate expressed as ω/π and an Arrhenius-like probability of successful hopping $P(T) \propto \exp(-E_a/k_B T)$, with E_a denoting the activation energy scale. The $D(\omega)$ of the localized modes is thus expressed as:

$$D(\omega) = \frac{\alpha^2\omega}{\pi}P(T) \quad (2)$$

Integrating over the vibrational spectra, the lattice thermal conductivity based on the hopping model is written as:

$$\begin{aligned} \kappa_{ph}(T) = k_B(n - n_E) \sum_j v_j^2 \left(\frac{T}{\theta_{c_j}}\right)^3 \int_0^{\frac{\theta_{c_j}}{T}} \frac{x^4 e^x}{(e^x - 1)^2} \tau(x, T) dx \\ + 3n_E k_B \frac{x_E^2 e^{x_E}}{(e^{x_E} - 1)^2} \alpha^2 \frac{\pi}{\omega_E} P(T) \end{aligned} \quad (3)$$

where $x = \hbar\omega/k_B T$, ω_c is the cut-off frequency between the propagating phonons and localized modes, n is number density of atoms, n_E is the number density of Einstein

oscillators, v_j is the group velocity of acoustic branch j . θ_{cj} is similar to the Debye temperature of branch j , defined as $\theta_{cj} = \hbar\omega_{cj}/k_B$. ω_E denotes the average frequency of Einstein oscillators. More details of the hopping model are listed in Supplemental Material S5. Fig. 4c-d show that the hopping model well captures the glass-like temperature dependence of κ_z . Our measurement also showed a peak (Figs. 4c and 4d) at T_{CDW} in temperature-dependent κ_z , which supports recent identifications of 3D CDW lattice distortions^{17,18}. Based on the proposed hopping model, the excess κ_z contributed by the CDW phase change can be estimated from the peak heights, with $0.08 \text{ W m}^{-1} \text{ K}^{-1}$ and $0.14 \text{ W m}^{-1} \text{ K}^{-1}$ for RbV_3Sb_5 and CsV_3Sb_5 , respectively.

In summary, this work systematically measures the temperature-dependent thermal conductivity of the kagome metals AV_3Sb_5 ($A = \text{Rb}, \text{Cs}$) using pump-probe thermoreflectance techniques. The two kagome metals exhibit moderate in-plane thermal conductivities at room temperature, with $12 \text{ W m}^{-1} \text{ K}^{-1}$ of RbV_3Sb_5 and $8.8 \text{ W m}^{-1} \text{ K}^{-1}$ of CsV_3Sb_5 . The cross-plane thermal conductivities are determined as $0.72 \text{ W m}^{-1} \text{ K}^{-1}$ and $0.49 \text{ W m}^{-1} \text{ K}^{-1}$ for RbV_3Sb_5 and CsV_3Sb_5 , respectively. The low κ_z arises from strongly reduced phonon group velocity associated with weak interlayer bonding. Unique glass-like temperature dependence of κ_z is observed where a phonon hopping transport model is proposed. Our measurement is consistent with recent discoveries that the CDW phase transition in AV_3Sb_5 is of order-disorder type. Sudden increase in κ_z has also been experimentally observed at T_{CDW} , supporting recent identifications of 3D CDW transitions where the lattice distortions are modulated in the cross-plane direction. The measurements of the thermal conductivities of AV_3Sb_5 serve as an important benchmark for understanding thermal transport in material systems with order-disorder phase transitions and dynamic instabilities.

Acknowledgments

X.Q. and R.Y. acknowledge support from National Key R & D Project from Ministry of Science and Technology of China (Grant No. 2022YFA1203100) and National Natural Science Foundation of China (NSFC Grant No. 52276065). Z.W acknowledges support from the National Natural Science Foundation of China (Grant No. 92065109), the National Key R&D Program of China (Grant Nos. 2020YFA0308800, 2022YFA1403401), the Beijing Natural Science Foundation (Grant Nos. Z190006, Z210006). J.Z. thanks support from National Natural Science Foundation of China (NSFC Grant No. 51976025). Y.P. acknowledges the support from Cross-Discipline Ph.D. Education Plan. Z. W. thanks the Analysis & Testing Center at BIT for assistance in facility support. The authors declare no conflict of interest.

References

1. Ye, L. et al. Massive Dirac fermions in a ferromagnetic kagome metal. *Nature* **555**, 638–642 (2018).
2. Kang, M. et al. Dirac fermions and flat bands in the ideal kagome metal FeSn. *Nat. Mater.* **19**, 163–169 (2020).
3. Yan, S., Huse, D. A. & White, S. R. Spin-Liquid Ground State of the $S = 1/2$ Kagome Heisenberg Antiferromagnet. *Science* **332**, 1173–1176 (2011).
4. Isakov, S. V., Wessel, S., Melko, R. G., Sengupta, K. & Kim, Y. B. Hard-Core Bosons on the Kagome Lattice: Valence-Bond Solids and Their Quantum Melting. *Phys. Rev. Lett.* **97**, 147202 (2006).
5. Ko, W.-H., Lee, P. A. & Wen, X.-G. Doped kagome system as exotic superconductor. *Phys. Rev. B* **79**, 214502 (2009).
6. Guo, H. & Franz, M. Topological insulator on the kagome lattice. *Phys. Rev. B* **80**, 113102 (2009).
7. Ortiz, B. R. et al. New kagome prototype materials: discovery of KV_3Sb_5 , RbV_3Sb_5 , and CsV_3Sb_5 . *Phys. Rev. Mater.* **3**, 094407 (2019).
8. Ortiz, B. R. et al. CsV_3Sb_5 : A Z-2 Topological Kagome Metal with a Superconducting Ground State. *Phys. Rev. Lett.* **125**, 247002 (2020).
9. Ortiz, B. R. et al. Superconductivity in the Z-2 kagome metal KV_3Sb_5 . *Phys. Rev. Mater.* **5**, 034801 (2021).
10. Zhao, H. et al. Cascade of correlated electron states in the kagome superconductor CsV_3Sb_5 . *Nature* **599**, 216–221 (2021).
11. Fu, Y. et al. Quantum Transport Evidence of Topological Band Structures of Kagome Superconductor CsV_3Sb_5 . *Phys. Rev. Lett.* **127**, 207002 (2021).
12. Zhou, X. et al. Anomalous thermal Hall effect and anomalous Nernst effect of CsV_3Sb_5 . *Phys. Rev. B*

- 105**, 205104 (2022).
13. Li, H. et al. Rotation symmetry breaking in the normal state of a kagome superconductor KV_3Sb_5 . *Nat. Phys.* **18**, 265–270 (2022).
 14. Kang, M. et al. Charge order landscape and competition with superconductivity in kagome metals. *Nat. Mater.* **22**, 186–193 (2023).
 15. Li, Y. et al. Tuning the competition between superconductivity and charge order in the kagome superconductor $Cs(V_{1-x}Nb_x)_3Sb_5$. *Phys. Rev. B* **105**, L180507 (2022).
 16. Kato, T. et al. Fermiology and Origin of T_c Enhancement in a Kagome Superconductor $Cs(V_{1-x}Nb_x)_3Sb_5$. *Phys. Rev. Lett.* **129**, 206402 (2022).
 17. Liang, Z. et al. Three-Dimensional Charge Density Wave and Surface-Dependent Vortex-Core States in a Kagome Superconductor CsV_3Sb_5 . *Phys. Rev. X* **11**, 031026 (2021).
 18. Ortiz, B. R. et al. Fermi Surface Mapping and the Nature of Charge-Density-Wave Order in the Kagome Superconductor CsV_3Sb_5 . *Phys. Rev. X* **11**, 041030 (2021).
 19. Yin, Q. et al. Superconductivity and Normal-State Properties of Kagome Metal RbV_3Sb_5 Single Crystals. *Chin. Phys. Lett.* **38**, 037403 (2021).
 20. Tan, H., Liu, Y., Wang, Z. & Yan, B. Charge Density Waves and Electronic Properties of Superconducting Kagome Metals. *Phys. Rev. Lett.* **127**, 046401 (2021).
 21. Chen, H. et al. Roton pair density wave in a strong-coupling kagome superconductor. *Nature* **599**, 222–228 (2021).
 22. Shumiya, N. et al. Intrinsic nature of chiral charge order in the kagome superconductor RbV_3Sb_5 . *Phys. Rev. B* **104**, 035131 (2021).
 23. Jiang, Y. et al. Unconventional chiral charge order in kagome superconductor KV_3Sb_5 . *Nat. Mater.* **20**,

- 1353–1357 (2021).
24. Xiao, Q. et al. Coexistence of multiple stacking charge density waves in kagome superconductor CsV_3Sb_5 . *Phys. Rev. Res.* **5**, L012032 (2023).
 25. Li, H. et al. Observation of Unconventional Charge Density Wave without Acoustic Phonon Anomaly in Kagome Superconductors AV_3Sb_5 ($A = \text{Rb}, \text{Cs}$). *Phys. Rev. X* **11**, 031050 (2021).
 26. Subires, D. et al. Order-disorder charge density wave instability in the kagome metal (Cs, Rb) V_3Sb_5 . *Nat. Commun.* **14**, 1015 (2023).
 27. Kwok, R. S. & Brown, S. E. Thermal conductivity of the charge-density-wave systems $\text{K}_{0.3}\text{MoO}_3$ and $(\text{TaSe}_4)_2\text{I}$ near the Peierls transition. *Phys. Rev. Lett.* **63**, 895–898 (1989).
 28. Lee, P. A., Rice, Tjv. & Anderson, P. W. CONDUCTIVITY FROM CHARGE OR SPIN DENSITY WAVES. *Solid State Commun.* **14**, 703–709 (1997).
 29. Núñez-Regueiro, M. D., Lopez-Castillo, J. M. & Ayache, C. Thermal Conductivity of 1T-TaS₂ and 2H-TaSe₂. *Phys. Rev. Lett.* **55**, 1931–1934 (1985).
 30. Liu, H. et al. Anomalously Suppressed Thermal Conduction by Electron-Phonon Coupling in Charge-Density-Wave Tantalum Disulfide. *Adv. Sci.* **7**, 1902071 (2020).
 31. Gerber, S. et al. Three-dimensional charge density wave order in $\text{YBa}_2\text{Cu}_3\text{O}_{6.67}$ at high magnetic fields. *Science* **350**, 949–952 (2015).
 32. Wang, Z. et al. Three-dimensional charge density wave observed by angle-resolved photoemission spectroscopy in 1T-VSe₂. *Phys. Rev. B* **104**, 155134 (2021).
 33. Yang, K. et al. Charge fluctuations above T_{CDW} revealed by glasslike thermal transport in kagome metals CsV_3Sb_5 ($A = \text{K}, \text{Rb}, \text{Cs}$). *Phys. Rev. B* **107**, 184506 (2023).
 34. Jiang, P., Qian, X. & Yang, R. Tutorial: Time-domain thermoreflectance (TDTR) for thermal property

- characterization of bulk and thin film materials. *J. Appl. Phys.* **124**, 161103 (2018).
35. Cahill, D. G., Watson, S. K. & Pohl, R. O. Lower limit to the thermal conductivity of disordered crystals. *Phys. Rev. B* **46**, 6131–6140 (1992).
 36. Wang, Z. et al. Electronic nature of chiral charge order in the kagome superconductor CsV₃Sb₅. *Phys. Rev. B* **104**, 075148 (2021).
 37. Cahill, D. G. Analysis of heat flow in layered structures for time-domain thermoreflectance. *Rev. Sci. Instrum.* **75**, 5119–5122 (2004).
 38. Schmidt, A. J., Cheaito, R. & Chiesa, M. A frequency-domain thermoreflectance method for the characterization of thermal properties. *Rev. Sci. Instrum.* **80**, 094901 (2009).
 39. Qian, X., Gu, X., Yang, R. & Yang, R. Probing Anisotropic Thermal Conductivity of Transition Metal Dichalcogenides MX₂ (M = Mo, W and X = S, Se) using Time-Domain Thermoreflectance. *Adv. Mater.* **29**, 1701068 (2017).
 40. Sun, B. et al. Temperature Dependence of Anisotropic Thermal-Conductivity Tensor of Bulk Black Phosphorus. *Adv. Mater.* **29**, 1603297 (2017).
 41. Jiang, P., Qian, X. & Yang, R. Time-domain thermoreflectance (TDTR) measurements of anisotropic thermal conductivity using a variable spot size approach. *Rev. Sci. Instrum.* **88**, 074901 (2017).
 42. Jiang, P., Qian, X., Yang, R. & Lindsay, L. Anisotropic thermal transport in bulk hexagonal boron nitride. *Phys. Rev. Mater.* **2**, 064005 (2018).
 43. Jang, H., Ryder, C. R., Wood, J. D., Hersam, M. C. & Cahill, D. G. 3D Anisotropic Thermal Conductivity of Exfoliated Rhenium Disulfide. *Adv. Mater.* **29**, 1700650 (2017).
 44. Qian, X., Ding, Z., Shin, J., Schmidt, A. J. & Chen, G. Accurate measurement of in-plane thermal conductivity of layered materials without metal film transducer using frequency domain

- thermoreflectance. *Rev. Sci. Instrum.* **91**, 064903 (2020).
45. Park, K. H., Mohamed, M., Aksamija, Z. & Ravaioli, U. Phonon scattering due to van der Waals forces in the lattice thermal conductivity of Bi₂Te₃ thin films. *J. Appl. Phys.* **117**, 015103 (2015).
 46. Mohr, M. et al. Phonon dispersion of graphite by inelastic x-ray scattering. *Phys. Rev. B* **76**, 035439 (2007).
 47. Lindroth, D. O. & Erhart, P. Thermal transport in van der Waals solids from first-principles calculations. *Phys. Rev. B* **94**, 115205 (2016).
 48. Jang, H., Wood, J. D., Ryder, C. R., Hersam, M. C. & Cahill, D. G. Anisotropic Thermal Conductivity of Exfoliated Black Phosphorus. *Adv. Mater.* **27**, 8017–8022 (2015).
 49. Guo, R. et al. Electrostatic interaction determines thermal conductivity anisotropy of Bi₂O₂Se. *Cell Rep. Phys. Sci.* **2**, 100624 (2021).
 50. Wang, Y., Liebig, C., Xu, X. & Venkatasubramanian, R. Acoustic phonon scattering in Bi₂Te₃/Sb₂Te₃ superlattices. *Appl. Phys. Lett.* **97**, 083103 (2010).
 51. Wang, Y., Xu, N., Li, D. & Zhu, J. Thermal Properties of Two-Dimensional Layered Materials. *Adv. Funct. Mater.* **27**, 1604134 (2017).
 52. Callaway, J. Model for Lattice Thermal Conductivity at Low Temperatures. *Phys. Rev.* **113**, 1046–1051 (1959).

Supplementary Materials: Glass-like Cross-plane Thermal Conductivity of Kagome Metals RbV_3Sb_5 and CsV_3Sb_5

Yu Pang¹, Jinjin Liu^{2,5}, Zeyu Xiang¹, Xuanhui Fan³, Jie Zhu^{3,*}, Zhiwei Wang^{2,5,6,*},
Yugui Yao^{2,5,6}, Xin Qian^{1,*}, Ronggui Yang^{1,4,*}

¹ School of Energy and Power Engineering, Huazhong University of Science and Technology, Wuhan 430074, China

² Centre for Quantum Physics, Key Laboratory of Advanced Optoelectronic Quantum Architecture and Measurement (MOE), School of Physics, Beijing Institute of Technology, Beijing 100081, China

³ School of Energy and Power Engineering, Dalian University of Technology, Dalian 116024, China

⁴ State Key Laboratory of Coal Combustion, Huazhong University of Science and Technology, Wuhan 430074, China

⁵ Beijing Key Lab of Nanophotonics and Ultrafine Optoelectronic Systems, Beijing Institute of Technology, Beijing 100081, China

⁶ Material Science Center, Yangtze Delta Region Academy of Beijing Institute of Technology, Jiaxing 314011, China

*Corresponding emails: zhujie@dlut.edu.cn; zhiweiwang@bit.edu.cn;
xinqian21@hust.edu.cn; ronggui@hust.edu.cn

Contents

S1. Anisotropic thermal conductivity measurements

S2. Sensitivity analysis

S3. Uncertainty analysis

S4. Estimation of κ_e using Wiedemann-Franz law

S5. Hopping model for cross-plane thermal transport

S1. Anisotropic thermal conductivity measurements

We combine TDTR and FDTR to simultaneously obtain κ_z and κ_r of kagome metals AV_3Sb_5 ($A = \text{Rb}, \text{Cs}$)^{1,2} (Figure S1), where TDTR is used to determine κ_z and FDTR is used to determine κ_r . The root-mean-square spot radius w are 20 μm (TDTR) and 3 μm (FDTR), obtained by fitting the in-phase signal as a function of offset distances between the pump and the probe beams³. We use the four-point probe to characterize the electric conductivity of metal transducers, and the thermal conductivity is then estimated using the Wiedemann-Franz law. The thickness h of Au and Al transducers is measured by the DektakXT profilometer (Bruker, USA). The temperature-dependent volumetric heat capacity C of AV_3Sb_5 is taken from the reported theoretical fittings based on Physical Property Measurement System (PPMS) measurements⁴. Table S1 summarizes the parameters of the Al/ AV_3Sb_5 and Au/ AV_3Sb_5 samples for TDTR and FDTR measurements at room temperature, respectively.

Table S1. Parameters for TDTR/FDTR measurements at room temperature.

Layer	κ_z ($\text{W m}^{-1} \text{K}^{-1}$)	κ_r ($\text{W m}^{-1} \text{K}^{-1}$)	h (nm)	w (μm)	C ($\text{MJ m}^{-3} \text{K}^{-1}$)	G ($\text{MW m}^{-2} \text{K}^{-1}$)
Al	150	150	109	20	2.44	60
Au	220	220	100	3	2.49	30
RbV ₃ Sb ₅	0.72	8.8	-	-	1.47	-
CsV ₃ Sb ₅	0.49	12	-	-	1.50	-

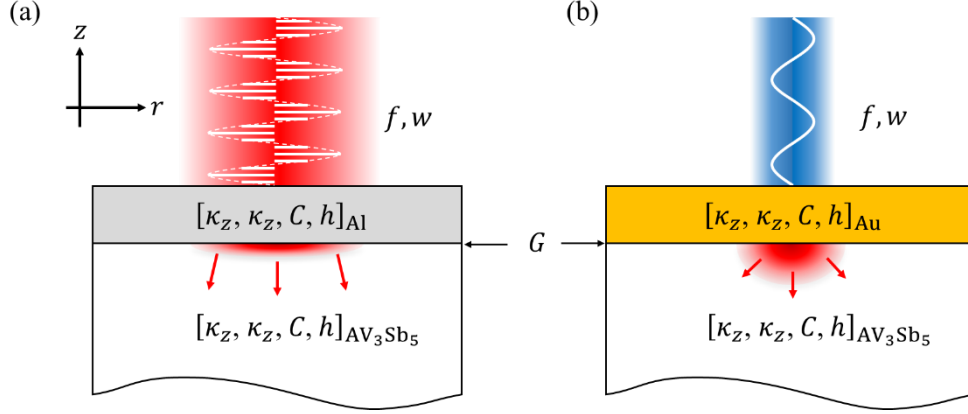


Fig. S1. Schematic of measuring the anisotropic thermal conductivity of AV_3Sb_5 using (a) TDTR and (b) FDTR.

S2. Sensitivity analysis

We perform sensitivity analysis to determine experimental settings (modulation frequency range, laser spot radius, etc.) for characterizing anisotropic thermal conductivity. The sensitivity in pump-probe measurement is defined as:

$$S_x^y = \frac{\partial \ln y}{\partial \ln x} \quad (S1)$$

where y denotes the signal (amplitude or phase) and x represents the parameter of interest. Figure. S2 shows sensitivity analysis of CsV_3Sb_5 using TDTR and FDTR measurements with different experiment setups at 300 K. Parameters for computing experimental sensitivities are shown in Table S1. Fig. S2a-b shows the sensitivity curves of the TDTR system implemented in this work. With a root-mean-square spot radius w of 20 μm , the TDTR measurement is primarily sensitive to κ_z but insensitive to κ_r . Fig. S2c-d shows that the TDTR system implemented in our lab has low sensitivity to the in-plane thermal conductivity, even with a tightly focused laser spot with a radius of 4 μm and a modulation frequency of 1.2 MHz⁵. We, therefore, use the FDTR with the lowest modulation frequency of 10 kHz and a small w of 3 μm to achieve high sensitivity to the in-plane thermal conductivity of AV_3Sb_5 , as shown in Fig. S2e-f.

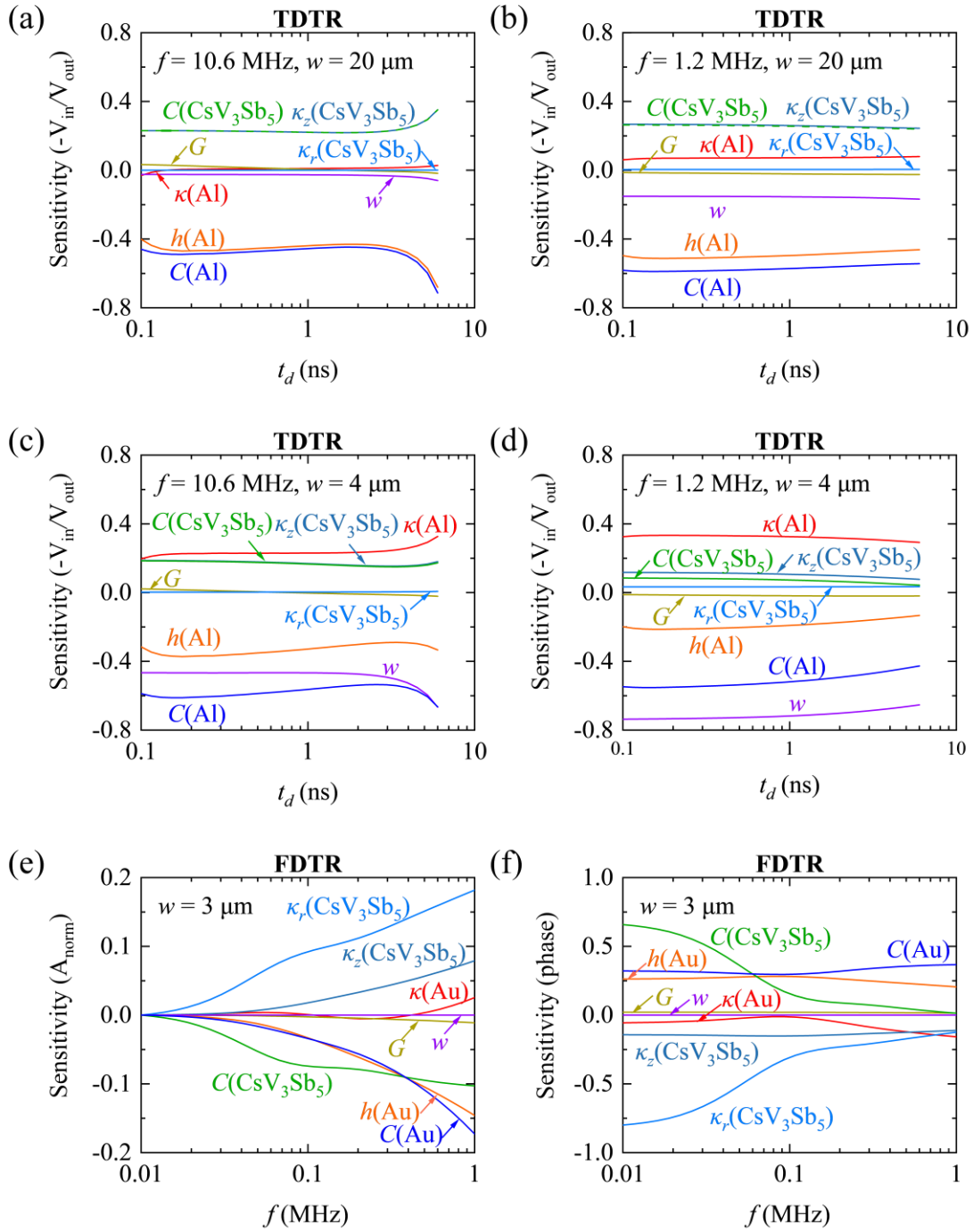


Fig. S2. Sensitivities of CsV_3Sb_5 using TDTR or FDTR measurements with different experiment setups: TDTR using $-V_{\text{in}}/V_{\text{out}}$ signal (a) with $f = 10.6$ MHz and $w = 20$ μm , (b) with $f = 1.2$ MHz and $w = 20$ μm , (c) with $f = 10.6$ MHz and $w = 4$ μm , (d) with $f = 1.2$ MHz and $w = 4$ μm ; FDTR using (e) A_{norm} and (f) phase signal with $f = 0.1$ -1 MHz and $w = 3$ μm . Sensitivities of $\kappa_z(\text{CsV}_3\text{Sb}_5)$ are higher than >0.2 in TDTR measurement using a large beam size, together with $\kappa_r(\text{CsV}_3\text{Sb}_5)$ fully suppressed less than 0.01 (sensitivity at $f = 3.1$ MHz is consistent but not shown here for clarity).

S3. Uncertainty analysis

We use the multivariate error propagation formula based on Jacobi matrices for uncertainty analysis^{6,7}. The variance of unknown parameters \mathbf{X}_U is calculated as:

$$\text{Var}[\mathbf{X}_U] = (\mathbf{J}_U^T \mathbf{J}_U)^{-1} \mathbf{J}_U^T (\text{Var}[\mathbf{y}] + \mathbf{J}_P \text{Var}[\mathbf{X}_P] \mathbf{J}_P^T) \mathbf{J}_U (\mathbf{J}_U^T \mathbf{J}_U)^{-1} \quad (\text{S2})$$

where the superscript T represents the matrix transpose, \mathbf{J}_U and \mathbf{J}_P are the Jacobian matrices correlating the signal \mathbf{y} and the unknown parameters \mathbf{X}_U or control parameters \mathbf{X}_P , respectively. In this work, the control parameters \mathbf{X}_P include the root-mean-square radius w , the properties of the metal transducers (κ , C , and h), and the heat capacity of AV_3Sb_5 . Typical uncertainty levels are: 10% for $\kappa(\text{Al})/\kappa(\text{Au})$, 3% for $C(\text{Al})/C(\text{Au})$ and $C(\text{AV}_3\text{Sb}_5)$, 4% for $h(\text{Al})/h(\text{Au})$, and 5% for w . For TDTR measurements, the vector of unknown parameters \mathbf{X}_U include κ_z of AV_3Sb_5 and the interface conductance G . After TDTR measurements are performed, κ_z is included as the control parameter X_P when performing uncertainty analysis of FDTR, and \mathbf{X}_U of FDTR only includes κ_r and G . Table S2 summarizes the $\text{Var}[\mathbf{X}_U]$ for TDTR and FDTR fitting of CsV_3Sb_5 at 300 K. The uncertainties (2σ) of each unknown parameter can be calculated as the square root of the diagonal elements of the matrix $\text{Var}[\mathbf{X}_U]$.

Table. S2. Covariance matrices $\text{Var}[\mathbf{X}_U]$ of the experimental data measured upon TDTR and FDTR for CsV_3Sb_5 at 300 K, fitted using the multilayered heat transfer model. The units are κ_z ($\text{W m}^{-1} \text{K}^{-1}$), κ_r ($\text{W m}^{-1} \text{K}^{-1}$) and G ($\text{MW m}^{-2} \text{K}^{-1}$).

TDTR	G	κ_z
G	176	-0.129
κ_z	-0.129	0.0049
Best-fit	60	0.49
Uncertainty	21.8 %	14.3 %
FDTR	G	κ_r
G	2600	-27.4
κ_r	-27.4	2.3
Best-fit	30	8.8
Uncertainty	174%	17.1%

S4. Estimation of κ_e using Wiedemann-Franz law

The electron thermal conductivity κ_e and phonon thermal conductivity κ_{ph} are obtained using the Wiedemann-Franz law $\kappa_e = LT/\rho$ where L and ρ are Lorenz number and electrical resistivity, respectively. More specifically, in-plane electrical resistivity ρ_r of AV_3Sb_5 is first acquired using a physical property measurement system (PPMS), over a temperature range of 80-300 K. The high-temperature (300-400 K) ρ_r is estimated through linear extrapolation of the measured ρ_r above Debye temperature (175.5 K for RbV_3Sb_5 , 142 K for CsV_3Sb_5 [8]), in which ρ_r is linearly dependent on temperature [9], as shown in as shown in Fig. S3a. Cross-plane electrical resistivity ρ_z is subsequently estimated using the formula $\rho_z = \alpha\rho_r$, where α is the ratio between ρ_z and ρ_r . The α has been reported to be about 600 and nearly temperature-independent¹⁰. Once κ_e along the in-plane and cross-plane directions (shown in Fig. S3b-c) are determinate from ρ , phonon thermal conductivity κ_{ph} is acquired by subtracting κ_e from the measured thermal conductivity κ .

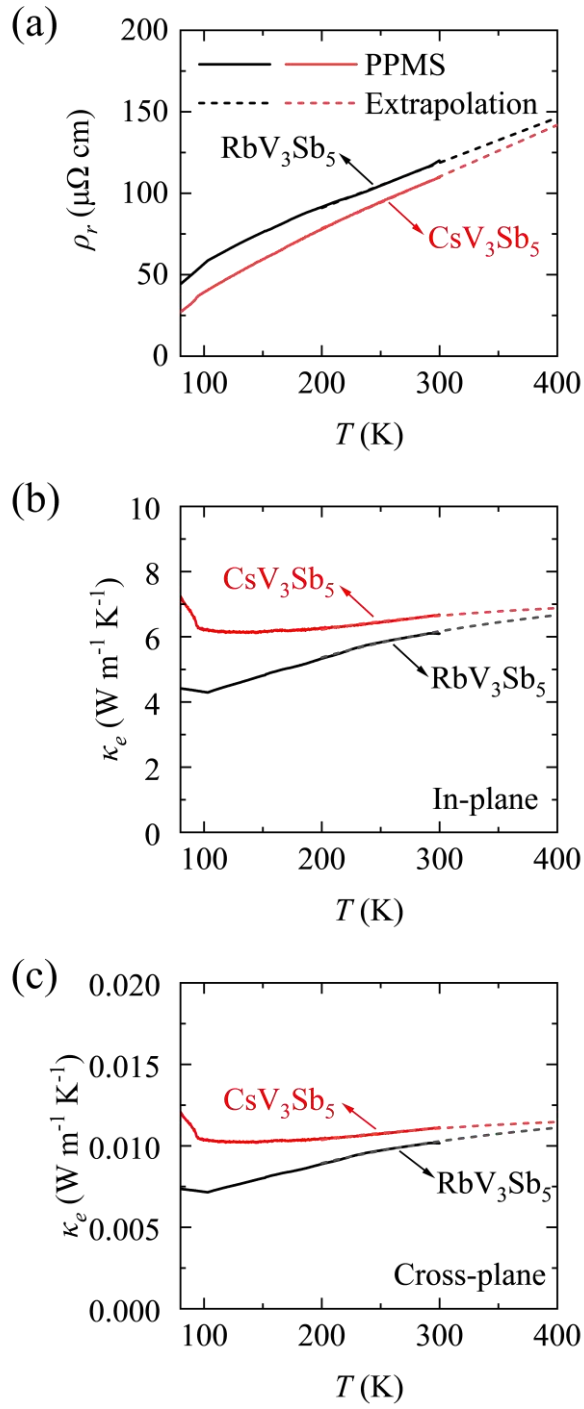


Fig. S3. (a) in-plane electrical resistivity, (b) in-plane electron thermal conductivity, and (c) cross-plane electron thermal conductivity of AV_3Sb_5 ($A = \text{Rb}, \text{Cs}$).

S5. Hopping model for cross-plane thermal transport

In order to describe the glass-like cross-plane thermal transport, a hopping model is proposed in this work, inspired by the recent observation of localized vibration modes driving the order-disorder CDW phase transition in AV_3Sb_5 ¹¹. Our hopping model separately treats the propagating low-frequency phonons and the high-frequency localized modes. The low-frequency phonons are described by the Callaway model with the Debye approximation, while the localized high-frequency modes can be treated as Einstein oscillators. Therefore, the vibrational density of states is written as:

$$g(\omega) = \begin{cases} \frac{3\omega^2}{2\pi^2 v_s^3}, & \omega < \omega_c \\ 3n_E \delta(\omega - \omega_E), & \omega > \omega_c \end{cases} \quad (\text{S3})$$

where ω_c is the cut-off frequency between the propagating phonons and localized modes, v_s is the averaged acoustic velocity, and n_E denotes the number density of Einstein oscillators. With the Debye approximation, the total number of propagating modes below ω_c should equal $3(n - n_E)$, therefore:

$$\int_0^{\omega_c} g(\omega) d\omega = 3(n - n_E) \quad (\text{S4})$$

which results in an explicit expression correlating n_E and ω_c :

$$\omega_c = [6\pi^2 v_s^3 (n - n_E)]^{1/2} \quad (\text{S5})$$

where n is the number density of atoms. Following Allen-Feldman's definition of spectral thermal diffusivity $D(\omega)$, the thermal conductivity can be computed by integrating $C(\omega)D(\omega)$ over the vibrational spectrum. For low-frequency propagating phonons, $D(\omega)$ is simply $v(\omega)^2 \tau(\omega)/3$ from the phonon-gas model, with $\tau(\omega)$ denoting the relaxation time. The propagation of the localized modes can be described by a random walk theory¹², where the $D(\omega)$ is determined by the hopping length α , hopping rates expressed as ω/π ¹³, and probability of a successful hopping P . Considering the structural fluctuation is driven by finite temperature, we phenomenologically describe the probability of successful hopping P using the

Arrhenius law $P = Ae^{-\frac{E_a}{k_B T}}$, where E_a is activation energy and A is the preexponential factor. Therefore, the $D(\omega)$ over the phonon spectrum is expressed as:

$$D(\omega) = \begin{cases} \frac{1}{3} v_s^2 \tau(\omega), & \omega < \omega_c \\ \alpha^2 \frac{\pi}{\omega} A e^{-\frac{E_a}{k_B T}}, & \omega > \omega_c \end{cases} \quad (\text{S5})$$

Substituting Eq. S(3-5) into Eq. (3) of the main text, we obtain calculated lattice thermal conductivity:

$$\begin{aligned} \kappa_{ph}(T) = k_B (n - n_E) \sum_j v_j^2 \left(\frac{T}{\theta_{cj}} \right)^3 \int_0^{\frac{\theta_{cj}}{T}} \frac{x^4 e^x}{(e^x - 1)^2} \tau(x, T) dx \\ + 3n_E k_B \frac{x_E^2 e^{x_E}}{(e^{x_E} - 1)^2} \alpha^2 \frac{\pi}{\omega_E} A e^{-\frac{E_a}{k_B T}} \end{aligned} \quad (\text{S6})$$

where $x = \frac{\hbar\omega}{k_B T}$, k_B is Boltzmann constant, $\tau(x, T)$ is spectral relaxation time, v_j is the group velocity of acoustic branch j . θ_{cj} is similar to the Debye temperature of branch j , defined as $\theta_{cj} = \hbar\omega_{cj}/k_B$. For cross-plane thermal transport, α is taken as the distance between the atomic layers. Table. S3 shows the related parameters for calculating the cross-plane thermal conductivity of AV_3Sb_5 using the hopping model, where v_j is derived from the phonon dispersion calculated by DFT⁸ and $\tau(x, T)$ is taken from Cahill-Pohl model¹⁴. The A defaults to 1 while n_E , ω_E and E_a are fitting parameters, with best-fit values listed Table. S3. The best-fit n_E is found very close to n , suggesting that the cross-plane thermal transport is dominated by the hopping mechanism, due to the small density of states of the low-frequency propagating modes. Figure. S4 shows that the hopping model proposed in this work accurately captures the glass-like temperature dependence of κ_z . The temperature-dependent κ_z by Cahill-Pohl model¹⁴ and the Callaway model¹⁵ are also included for comparison.

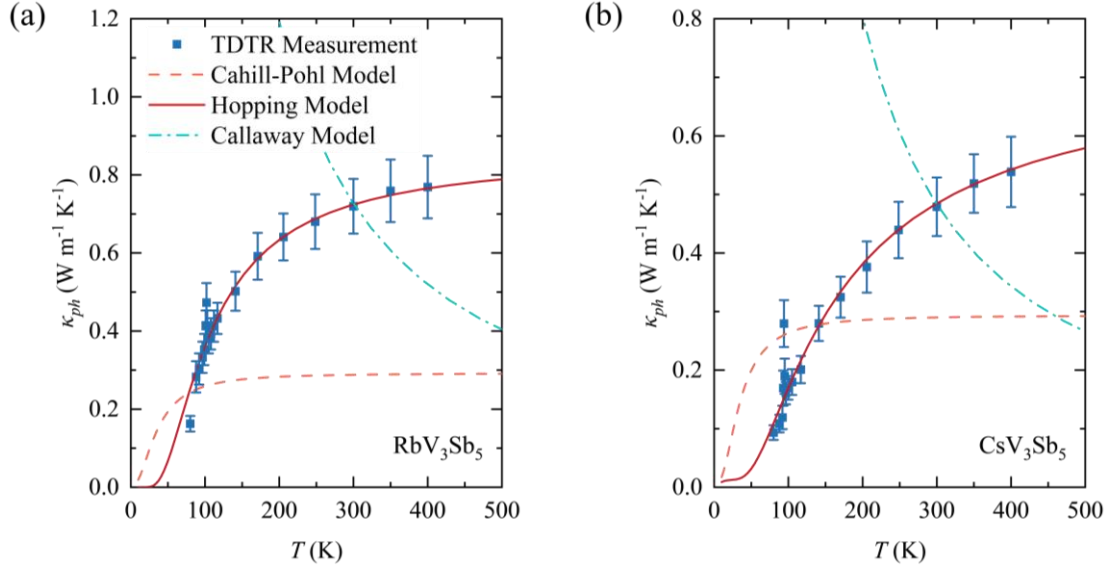


Fig. S4. Data fitting of TDTR-measured κ_{ph} along the cross-plane direction of (a) RbV_3Sb_5 and (b) CsV_3Sb_5 from 80 K to 400 K, using the hopping model, Cahill-Pohl model, and Callaway model.

Table. S3 Parameters of the hopping model fitting the TDTR-measured κ_{ph} of AV_3Sb_5

Sample	v_j	n	n_E	$\hbar\omega_E/k_B$	α	A	E_a/k_B
	m s^{-1}	(10^{28} m^{-3})	(10^{28} m^{-3})	(K)	(\AA)		(K)
RbV_3Sb_5	2200 (<i>l</i>)	3.83	3.80	257	2.27	1	35
	1210 (<i>t</i>)						
CsV_3Sb_5	1960 (<i>l</i>)	3.64	3.62	213	2.34	1	117
	1420 (<i>t</i>)						

References

1. Cahill, D. G. Analysis of heat flow in layered structures for time-domain thermoreflectance. *Rev. Sci. Instrum.* **75**, 5119–5122 (2004).
2. Schmidt, A. J., Cheaito, R. & Chiesa, M. A frequency-domain thermoreflectance method for the characterization of thermal properties. *Rev. Sci. Instrum.* **80**, 094901 (2009).
3. Feser, J. P. & Cahill, D. G. Probing anisotropic heat transport using time-domain thermoreflectance with offset laser spots. *Rev. Sci. Instrum.* **83**, 104901 (2012).
4. Yang, K. et al. Charge fluctuations above T_{CDW} revealed by glass-like thermal transport in kagome metals $A V_3 S b_5$ ($A = K, Rb, Cs$). *Phys. Rev. B* **107**, 184506 (2023).
5. Jiang, P., Qian, X. & Yang, R. Time-domain thermoreflectance (TDTR) measurements of anisotropic thermal conductivity using a variable spot size approach. *Rev. Sci. Instrum.* **88**, 074901 (2017).
6. Yang, J., Ziade, E. & Schmidt, A. J. Uncertainty analysis of thermoreflectance measurements. *Rev. Sci. Instrum.* **87**, 014901 (2016).
7. Qian, X., Jiang, P. & Yang, R. Anisotropic thermal conductivity of 4H and 6H silicon carbide measured using time-domain thermoreflectance. *Mater. Today Phys.* **3**, 70–75 (2017).
8. Tan, H., Liu, Y., Wang, Z. & Yan, B. Charge Density Waves and Electronic Properties of Superconducting Kagome Metals. *Phys. Rev. Lett.* **127**, 046401 (2021).
9. Kittel, C. *Introduction to solid state physics*. (Wiley, 2005).
10. Ortiz, B. R. et al. CsV_3Sb_5 : A Z-2 Topological Kagome Metal with a Superconducting Ground State. *Phys. Rev. Lett.* **125**, 247002 (2020).

11. Subires, D. et al. Order-disorder charge density wave instability in the kagome metal (Cs, Rb)V₃Sb₅. *Nat Commun* **14**, 1015 (2023).
12. Agne, M. T., Hanus, R. & Snyder, G. J. Minimum thermal conductivity in the context of *diffuson*-mediated thermal transport. *Energy Environ. Sci.* **11**, 609–616 (2018).
13. Einstein, A. Elementare Betrachtungen über die thermische Molekularbewegung in festen Körpern. *Ann. Phys.* **340**, 679–694 (1911).
14. Cahill, D. G., Watson, S. K. & Pohl, R. O. Lower limit to the thermal conductivity of disordered crystals. *Phys. Rev. B* **46**, 6131–6140 (1992).
15. Callaway, J. Model for Lattice Thermal Conductivity at Low Temperatures. *Phys. Rev.* **113**, 1046–1051 (1959).